www.vbripress.com/aml, DOI: 10.5185/amlett.2016.6174 Published online by the VBRI Press in 2016

Microstructural and phase analysis of Al based bulk metallic glass synthesized by mechanical alloying and consecutive spark plasma sintering with varying consolidation pressure

Ram S. Maurya, Ashutosh Sahu, Tapas Laha*

Department of Metallurgical and Materials Engineering, Indian Institute of Technology Kharagpur, Kharagpur 721302, India

*Corresponding author. Tel: (+91) 3222-283242; E-mail: laha@metal.iitkgp.ernet.in

Received: 15 September 2015, Revised: 07 December 2015 and Accepted: 03 January 2016

ABSTRACT

In the present work, $Al_{86}Ni_8Y_6$ and $Al_{86}Ni_8La_6$ powder blends were mechanically alloyed. $Al_{86}Ni_8Y_6$ yielded full amorphous structure (150 h); whereas $Al_{86}Ni_8La_6$ was partially amorphized after same duration of milling attributed to incomplete dissolution of solute 'La' in solvent 'Al'. DSC experiment showed wider glass transition temperature range of ~ 44 ^oC (T_x - T_g = 268 ^oC-224 ^oC) in $Al_{86}Ni_8Y_6$ amorphous powders; whereas no glass transition temperature was detected in $Al_{86}Ni_8La_6$ powders. Further, $Al_{86}Ni_8Y_6$ amorphous powders were consolidated via spark plasma sintering in the pressure range of 100-400 MPa. XRD and TEM analysis confirmed retention of larger fraction of amorphous phase in higher pressure sintered sample, attributed to suppression of mass transfer diffusion kinetics process. Higher pressure favored short range ordering leading to formation of various intermetallic phases; whereas comparatively faster diffusion in case of low pressure sintering promoted long range ordering forming nanocrystalline FCC-Al. Higher sintering pressure (say 400 MPa) consolidated sample resulted in better densification (~ 99 %) with improved inter-particle bonding and moreover, retention of larger volume fraction (~ 92 vol %) of amorphous phase with intermetallic nano-precipitates. Vickers microhardness test showed improvement in hardness with increasing sintering pressure attributed to higher fraction of retained amorphous phase and better inter-particle bonding.

Keywords: Al based amorphous alloy; mechanical alloying; spark plasma sintering; sintering pressure; microstructural evolution.

Introduction

Attributed to the absence of crystallinity and defects such as dislocations, grain boundaries and antiphase boundaries, glassy metallic materials exhibit excellent mechanical strength, good corrosion resistance, and exceptional electronic and magnetic properties [**1-2**]. Aluminium based glassy alloys possess excellent potential in structural applications owing to these alloys' high specific strength and good bending properties along with superb corrosion resistance [**3-5**]. Typical Al-based metallic glasses are Al–TM-RE systems (TM: early transition metals and RE: rare earth elements), containing 80–94 at % Al, 1–15 at % TM, and 3–20 at % RE [**6, 7**]. However, major barrier in fabricating Al-based bulk amorphous alloys by rapid solidification process is the necessity of extremely high cooling rate (i.e. 10^5-10^6 K/s) to suppress crystallization, attributed to very low glass transition temperature of these alloys [**3, 4, 8**]. Numerous studies have been performed on Al based ternary alloy systems (Al-TM-RE) such as Al-Ni-Y, Al-Ni-La, Al-Ni-Ce, Al-Fe-Ce, Al-Ni-Gd, Al-Ni-Sm etc. synthesized via rapid solidification process, where the alloy compositions were selected by adopting efficient atomic packing (EAP) and efficient cluster packing (ECP) model **[9-11**]. However, the maximum thickness of monolithic Al-based BMGs synthesized by rapid solidification is still limited to millimetre range, which limits the engineering application of these alloys [**4, 9, 10**].

Dimensional limitation of Al based glassy alloys synthesized by rapid solidification process promoted amorphous alloys synthesis via powder metallurgy route. Powder processing route (viz. mechanical alloying) offers various advantages, including large amount of powders synthesis with unique compositions without restriction of deep eutectic point in the phase diagram. Mechanically alloyed amorphous powders and consecutive consolidation through spark plasma sintering (SPS) could be an effective method to overcome the size limitation in synthesizing bulk glassy structure [**12-15**]. Generation of electric discharge between the powder particles, spark impact pressure on the particle surface, Joule heating and electric field enhanced diffusion makes SPS a highly efficient sintering technique. Quick heating rate and shorter sintering time in SPS process leads to faster sintering kinetics which can restrict unwanted phase transformation while achieving good densification. The SPS process also promotes abnormal

crystallization during sintering of amorphous powders and thus shows the ability to introduce nanometric phases in amorphous matrix which could act as a barrier during the process of deformation.

Povstugar *et al.* [**16**] reported the presence of Al nano-grains in mechanically alloyed and spark plasma sintered $Al_{85}Y_8Ni_5Co_2$ amorphous alloy. Formation of large Al grains [**17**] as well as nanometric Al_5Co_2 phase was reported by Li *et al.* [**18**] in SPS consolidated gas atomized $Al_{86}Ni_6Y_{4.5}Co_2La_{1.5}$ glassy powders attributed to abnormal crystallization during spark plasma sintering. Shen *et al.* reported significant reduction in crystalline phase formation along with a decrease in porosity in spark plasma sintered glassy $Fe_{65}Co_{10}Ga_5P_{12}C_4B_4$ alloy when sintering pressure was increased from 200 MPa to 300 MPa [**19**]. Kim *et al.* consolidated gas atomized $Cu_{47}Ti_{33}Zr_{11}Ni_6Sn_2Si_1$ powders via SPS at two different pressures (80 and 300 MPa) and found out that the increase in consolidation pressure improved the bonding between powders and suppressed formation of various crystalline phases [**20**].

The present study was involved in synthesizing fully amorphous Al-TM-RE powders by mechanical alloying and subsequent consolidation through spark plasma sintering at different pressures. The primary aim of the present research work was to explore the effect of sintering pressure on behaviour of amorphous phase retention along with various phase transformations (such as precipitation of intermetallics and formation of nanocrystalline Al) and densification behavior during sintering, and the consequent effect on the microhardness of the sintered alloy.

Experimental

Elemental powder blends of composition $Al_{86}Ni_8Y_6$ and $Al_{86}Ni_8La_6$ were obtained by mixing aluminium (99.5 %, -44 μm), nickel (99.996 %, -125 μm), yttrium (99.9 %, -420 μm) and La (99.9 %, -44 μm) powders. Wet mechanical alloying of $Al_{86}Ni_8Y_6$ and $Al_{86}Ni_8La_6$ powder mixtures was performed in hardened steel vials using hardened steel balls (diameter: 10 mm) using a planetary ball mill (PM 200, Retsch GmbH, Germany) at revolution per minute (RPM) of 300 and ball to powder weight ratio (BPR) of 15:1. $Al_{86}Ni_8Y_6$ alloy powders which yielded fully amorphous structure after 150 h of milling was consolidated in spark plasma sintering system (FUJI SPS 625, Fuji Electronic Industrial Co. Ltd., Japan) using tungsten carbide die-punch set. Sintering was carried out at varying pressure of 100 MPa to 400 MPa for 2 min at 400 ^oC with a heating rate of 100 ^oC/min.

Phase transformation in the mechanically alloyed powders and SPS consolidated bulk samples were investigated by performing X ray diffraction (Bruker D8 Advance diffractometer, Germany) using CuK_α (λ=1.54 Å) radiation. Differential scanning calorimetry (DSC Q20, TA Instruments, USA) was employed at heating rate of 20 ^oC/min to find out glass transition and higher temperature crystallization. Transmission electron microscopy (JEM-2100 LaB_6, 200 kV, JEOL USA, Inc.) was conducted to validate the formation of nanocrystalline, amorphous and other complex intermetallic phases in mechanically alloyed powders as well as consolidated samples. The effect of microstructural morphology and various phase evolution on mechanical properties of the SPS consolidated samples was studied by carrying out microhardness test (UHL VMHT - 001, Walter Uhl, Germany) at a load of 500 g.

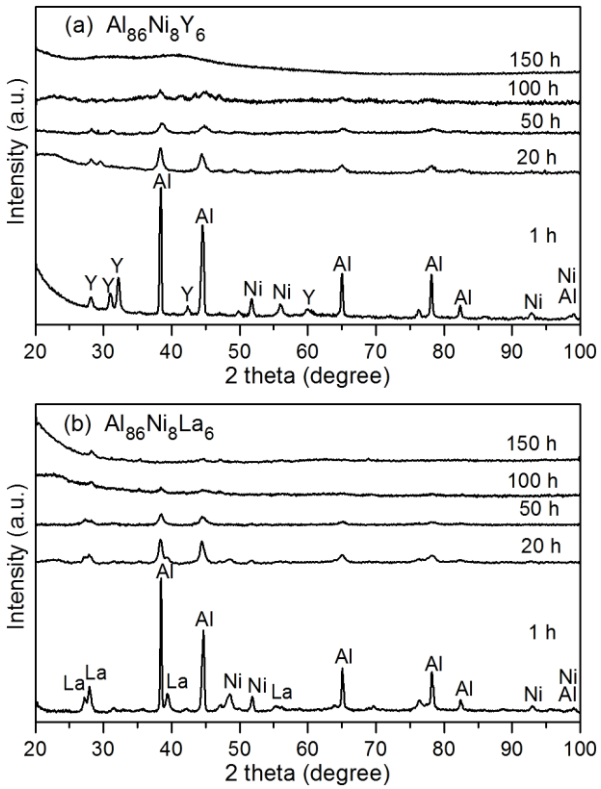

Fig. 1. XRD patterns of $Al_{86}Ni_8Y_6$ and $Al_{86}Ni_8La_6$ alloy powders, indicating microstructural deformation induced phase transformation at various intervals of mechanical alloying.

Results and discussion

Phase transformation in mechanically alloyed powders

Fig. 1 shows the XRD pattern of $Al_{86}Ni_8Y_6$ and $Al_{86}Ni_8La_6$ powders milled for various durations. Progressive milling time causes XRD peak broadening which signifies nanostructured alloy formation with lower crystallite size, distorted lattice parameter and higher lattice micro-strain [**21-22**]. XRD pattern of 20 h milled powders exhibited severe peak broadening and drastic decrease in peak intensities in comparison to 1 h milled powders signifying severe deformation and lattice micro-strain accumulation. XRD peaks broadening with continuous milling is also an indication of an increase in the amorphous phase traces. Progressive deformation increased strain energy in $Al_{86}Ni_8Y_6$ and $Al_{86}Ni_8La_6$ alloy system, which assisted in destabilizing the atomic periodicity. In this context, $Al_{86}Ni_8Y_6$ alloy exhibited fully amorphous structure after 150 h of milling as indicated by presence of diffused XRD hump (**Fig. 1a**) whereas $Al_{86}Ni_8La_6$ showed only partial amorphization (**Fig. 1b**). This could be attributed to the higher atomic radii of La (1.885 Å) in comparison to Y (1.831 Å) which made La dissolution difficult in solvent 'Al' based on Hume Rothery rule [**23**].

TEM images of $Al_{86}Ni_8Y_6$ and $Al_{86}Ni_8La_6$ alloy powders milled for 100 h and 150 h are shown in **Fig. 2**.

TEM image (**Fig. 2a**) of 100 h milled $Al_{86}Ni_8Y_6$ powders clearly demonstrates the presence of various crystalline precipitates along with amorphous phase indicating incomplete amorphization in this alloy composition. This result conforms to the XRD pattern of 100 h milled powders, which showed multiple peaks for intermetallic phases (**Fig 1a**). The TEM image of 150 h milled $Al_{86}Ni_8Y_6$ powders (**Fig. 2b**) exhibits completely featureless microstructure indicating presence of fully amorphous phase. Achieving complete amorphization in 150 h milled $Al_{86}Ni_8Y_6$ powders could further be confirmed from the totally diffused SAD pattern (**Fig. 2c**). $Al_{86}Ni_8La_6$ alloy powders milled for 100 h also clearly indicated crystalline phase (**Fig. 2d**). However, it can be noticed from the **Fig. 2e** that 150 h milled $Al_{86}Ni_8La_6$ powders was only partially amorphized even after milling of 150 h. The corresponding SAD pattern (**Fig. 2f**) showing various dots in diffused SAD pattern also supports this partial amorphization in 150 h milled powder containing 'La'.

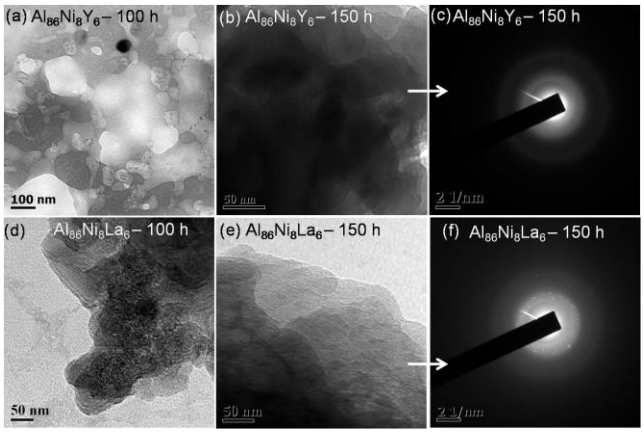

Fig. 2 TEM images and corresponding SAD patterns of 100 h and 150 h milled $Al_{86}Ni_8Y_6$ and $Al_{86}Ni_8La_6$ alloy powders, showing microstructural phase variation.

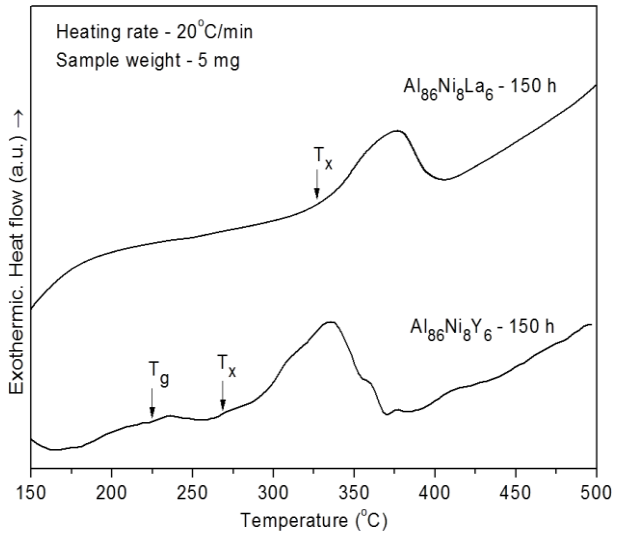

Fig. 3. DSC thermograms showing phase transitions in 150 h milled $Al_{86}Ni_8Y_6$ and $Al_{86}Ni_8La_6$ alloy powders.

DSC curve of 150 h milled $Al_{86}Ni_8Y_6$ and $Al_{86}Ni_8La_6$ alloy powders are shown in **Fig. 3**. $Al_{86}Ni_8Y_6$ amorphous powders exhibited glass transition (**Fig. 3a**, T_g ~ 224°C, T_x ~ 268°C, $T_g - T_x$ = 44 °C) followed by major crystallization related to nanocrystalline FCC-Al and Al rich intermetallic phase transition. On the other hand $Al_{86}Ni_8La_6$ alloy powders could not be amorphized fully as already depicted by corresponding XRD pattern (**Fig. 1b**) and TEM images (**Fig. 2(d-f)**), thus, glass transition temperature could not be detected. Broad hump related to nanocrystallization event of FCC-Al and other Al-rich complex phases could be observed (**Fig. 3b**).

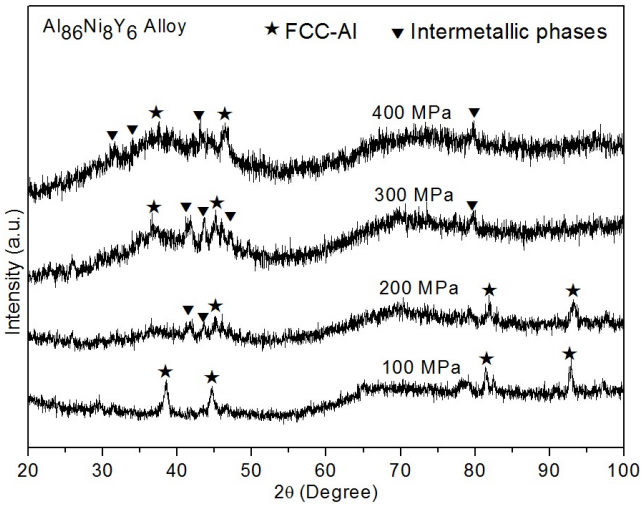

Fig. 4. XRD patterns of spark palsma sintered samples consolidated at varrying pressures showing variation in microstrutual phase evolution.

Microstructural phase analysis in spark plasma sintered alloys

XRD patterns of spark plasma sintered samples consolidated at varying pressure are shown in **Fig. 4**. As sintering pressure increased broad XRD hump became more pronounced and clear evincing higher fraction of retained amorphous phase. However, the appearance of multiple XRD peaks (2θ range of 35° - 50°, approximately) overlaid amorphous hump were observed in alloys sintered at higher pressure than 100 MPa, attributed to the evolution of nanocrystalline FCC-Al along with various intermetallic phases such as Al_3Ni, Al_3Y, Al_3Ni_2 and Al_2Y. In case of 100 MPa sintered sample, XRD hump diminished and sharp XRD peaks related to the nanocrystalline FCC-Al could clearly be observed (**Fig. 4**). The reason behind better retention of amorphous phase and formation of intermetallic phases in higher pressure (more than 100 MPa) sintered samples and formation of nanocrystalline Al in lower pressure (100 MPa) sintered sample is explained in the below paragraph.

Higher sintering pressure (more than 100 MPa) suppresses the long range diffusion of atoms and thus assists in retaining a higher fraction of amorphous phase [**24-26**]; whereas short range ordering may promote coupling of Al atoms with Ni or Y, following the topological criterion proposed by Miracle *et al.* [**27**], fostering intermetallic phase precipitation viz. Al_3Ni, Al_3Y, Al_3Ni_2, Al_2Y. On the other hand, long range diffusion in case of low pressure sintered sample promoted faster diffusion and thus formation of nanocrystalline FCC-Al in the 100 MPa sintered alloy was observed.

The literature survey indicated both improvement [**28**] and deterioration [**29**] in thermal stability (retention of amorphous structure) of amorphous alloy with increasing pressure. Jiang *et al.* reported enhanced crystallization temperature in Fe and Zr based bulk metallic glasses [**28, 30**] with increasing consolidation pressure. In this context, the present study also revealed that higher sintering pressure during SPS of amorphous $Al_{86}Ni_8Y_6$ powders suppressed the long range atomic diffusion and favoured only short range diffusion. Thus, better retention of amorphous phase along with the formation of traces of intermetallic phases was reported indicating improvement in thermal stability of amorphous alloys sintered at higher pressure.

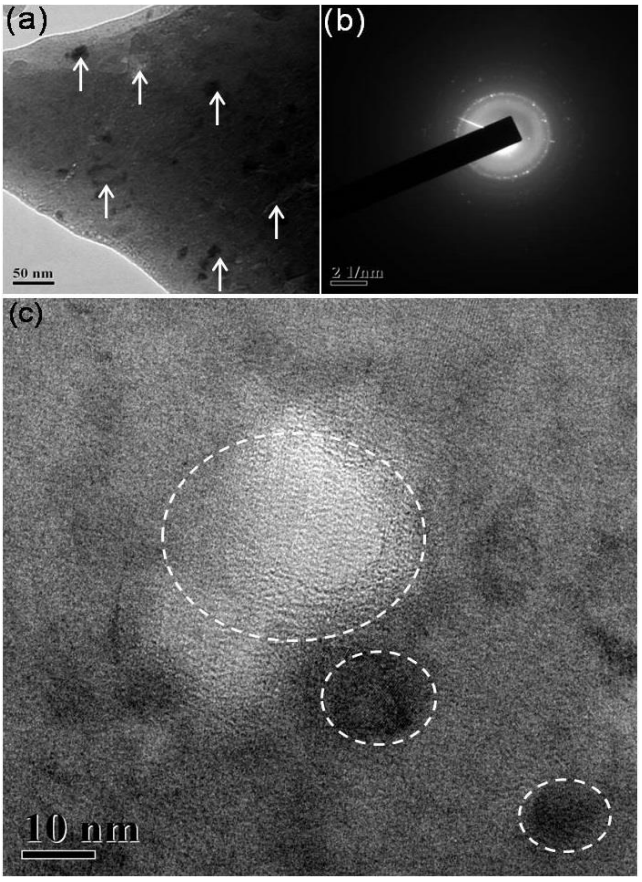

Fig. 5. (a) TEM micrograph of $Al_{86}Ni_8Y_6$ alloy sintered at 400 MPa showing nano-precipitates distributed in the amorphous matrix, (b) corresponding SAD pattern with diffused background and bright dots, revealing simultaneous presence of amorphous matrix and nano-precipitates and (c) high resolution image confirming the presence of amorphous matrix and nanocrystalline precipitates.

Transmission electron microscopy was performed to understand the various phase formation in $Al_{86}Ni_8Y_6$ alloy sintered at 400 MPa and images are shown in **Fig. 5**. Distribution of extremely fine nanocrystalline precipitate of sizes from 5-50 nm in amorphous matrix could clearly be observed as shown in **Fig. 5a**, indicated by white arrows. Corresponding partially diffused SAD pattern (**Fig. 5b**) with discrete spots and dotted ring confirmed the distribution of various precipitates in the amorphous matrix. For better understanding of the nanocrystalline precipitate distribution in amorphous matrix, high resolution TEM image was carried out and presented in **Fig. 5c**. It clearly depicts distorted lattice structure of amorphous phase along with regular lattice spacing related to crystalline precipitates.

Investigation of heating mechanism during SPS could focus some light on understanding of the sintering mechanism for amorphous powders. High current density and electric discharge between powder particles generate localized high temperature zones at powder contacts attributed to Joule heating [**31-33**]. Momentarily generated high localized temperature varies depending on particle morphology (viz. particle size, curvature and area of contact) [**33-34**]. These high temperature localized spots act as source of phase precipitation by boosting mass transfer diffusion process. Although there would be a huge number of such localised spots, but diffusion got suppressed and higher amorphous phase fraction was retained with increasing pressure; whereas lower pressure was not able to suppress the diffusion process leading to faster devitrification.

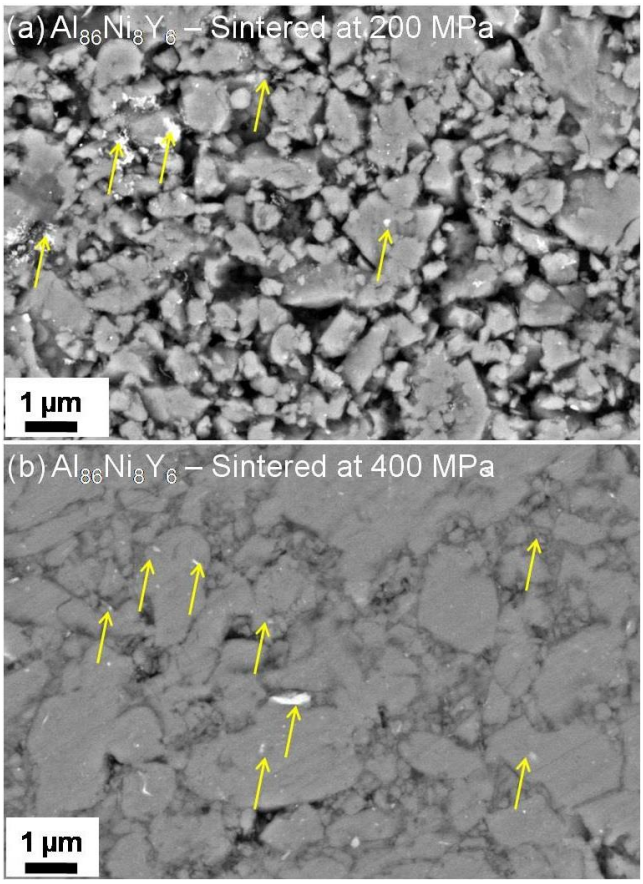

Fig. 6. SEM micrographs showing improvement in interparticle bonding and formation of intermetallics precipiates in spark plasma sintered $Al_{86}Ni_8La_6$ amorphous alloy with increase in sintering pressure from (a) 200 MPa to (b) 400 MPa.

Backscattered electron imaging (**Fig. 6**) of 200 MPa and 400 MPa pressure sintered samples was carried out to understand the densification behavior, interparticle bonding and noticing any intermetallic formation. Improvement in densification with increasing pressure can be envisaged from the images. Higher sintering pressure resulted in

higher stress concentration at particle which led to a better mass flow ensuring better inter-particle bonding and higher densification with reduction in the number and size of pores. Extremely fine nanocrystalline intermetallic precipitate could also be observed in 200 MPa (**Fig. 6a**) and 400 MPa (**Fig. 6b**) sintered alloys as indicated by yellow arrow mark, which was consistent with TEM (**Fig. 5**) and XRD results (**Fig. 4**).

Table 1. Microhardness of $Al_{86}Ni_8Y_6$ alloy sintered at various sintering pressures.

Sintering pressure (MPa)	100	200	300	400
Microhardness (GPa)	1.91±0.7	2.76±0.47	3.08±0.33	3.56±0.29

Effect of microstructure and phase evolution on mechanical properties

The microhardness test of various pressure sintered samples was conducted at load of 500gf and values are presented in the **Table 1**. Average microhardness values for samples consolidated at 100 MPa, 200 MPa, 300 MPa and 400 MPa were found to be 1.91±0.71 GPa, 2.76±0.47 GPa, 3.08±0.33 GPa and 3.56±0.29 GPa, respectively. Similar range of hardness (1.99 GPa - 3.45 GPa) was reported by Sasaki *et al.* [**35**] for $Al_{85}Ni_{10}La_5$ amorphous alloy with distributed nanocrystalline phases synthesized by SPS (with varying sintering temperature and pressure) of gas atomized amorphous powders. Amorphous alloy sintered at 400 MPa exhibited highest hardness attributed to (i) better inter-particle bonding (see **Fig. 6b**), (ii) high relative density (~ 99 %), (iii) higher amount of retained amorphous matrix (~ 92 vol %) (See **Fig. 5a**) and (iv) uniformly distributed *in- situ* nanocrystals in amorphous phase matrix, as shown in **Fig. 5a**.

Conclusion

In summary, $Al_{86}Ni_8Y_6$ and $Al_{86}Ni_8L_6$ alloy powders were mechanically alloyed, in which the previous one yielded fully amorphous structure; whereas later one was only partially amorphized after 150 h of milling, attributed to the incomplete dissolution of solute La in solvent Al. The DSC thermograms also indicated clear glass transition T_g at ~ 224 ^oC and T_x at ~ 268 ^oC and thus, a wider glass transition range of 44 ^oC in $Al_{86}Ni_8Y_6$ amorphous powders. No sign of glass transition was detected in case of partially amorphized $Al_{86}Ni_8L_6$ alloy powders. The fully amorphous powders of $Al_{86}Ni_8Y_6$ consolidated via spark plasma sintering at higher sintering pressure retained higher amount of amorphous phase; whereas a higher degree of crystallinity was observed in the lower pressure sintered sample. Better inter-particle bonding along with a higher fraction of retained amorphous phase and intermetallic nano-precipitates in the higher pressure sintered samples resulted in higher microhardness.

Acknowledgements

The author, T. Laha thankfully acknowledges the financial support obtained from the Science and Engineering Research Board, Department of Science & Technology, Government of India (SB/S3/ME/0044/2013) and Sponsored Research and Industrial Consultancy, Indian Institute of Technology Kharagpur, India (GAF).

Reference

1. Wang, W.H.; Dong, C.; Shek, C. H.; *Mater. Sci. Eng. R*, **2004**, *44*, 45.
2. Schuh, C.A.; Hufnagel, T.C.; Ramamurty, U.; *Acta. Mater.;* **2007**, *55*, 4067.
3. Inoue, A.; *Prog. Mater. Sci.*, **1998**, *43*, 65.
4. Yang, B. J.; Yao, J. H.; Zhang, J.; Yang, H. W.; Wang, J. Q.; Ma, E.; *Scripta Mater.*, **2009**, *61*, 423.
5. Sun, B.A.; Pan, M. X.; Zhao, D. Q.; Wang, W. H.; Xi, X. K.; Sandor, M. T.; Wu. Y.; *Scripta Mater.*, **2008**, *59*, 1159.
6. Zhang, Z.; Xiong, X. Z.; Zhou, W.; Lin, X.; Inoue, A.; Li, J. F.; *Intermetallics.*, **2013**, *42*, 23.
7. Zhang, Z.; Xiong, X. Z.; Zhou, W.; Li, J. F.; *J. Alloy. Comp.*, **2013**, *576*, *181*.
8. Wang, J. Q.; Dong, P.; Hou, W. L.; Chang, X. C.; Quan, M. X.; *J. Alloy. Comp.*, **2013**, *554*, 419.
9. Guo, F. Q.; Poon, S. J.; Shiflet, G. J.; *Scripta Mater.*, **2000**, *43*, 1089.
10. Ronto, V.; Battezzati, L.; Yavari, A. R.; Tonegaru, M.; Lupu, N.; Heunen, G.; *Scripta Mater.* **2004**, *50*, 839.
11. He, Y.; Poon, S. J.; Shiflet, G. J.; *Science*, **1988**, *241*, 640.
12. Li, X. P.; Yan, M.; Imai, H.; Kondoh, K.; Wang, J. Q.; Schaffer, G. B.; Qian, M.; *Mater. Sci. Eng. R*, **2013**, *568*, 155.
13. Li, X.P.; Yan, M.; Imai, H.; Kondoh, K.; Wang, J.Q.; Schaffer, G.B.; Qian, M.; *Mater. Sci. Eng. A*, **2013**, *568*, 155.
14. Deng, S.; Wanga, D.J.; Luo, Q.; Huang, Y.J.; Shen, J.; *Adv. Powder. Tech.*, **2015**, *26*, 1696. **DOI:**10.1016/j.apt.2015.10.009
15. Tan, Z.; Wang, L.; Xue, Y.; Cheng, X.; *Mater. Sci. Eng. A*, **2015**, *642*, 377.
16. Kim, J. S.; Povstugar, I. V.; Choi, P.P.; Yelsukov, E. P.; Kwon, Y. S.; *J. Alloy. Compd.*, **2009**, *486*, 511.
17. Li, X. P.; Wang, J. Q.; Yan, M.; Ji, G.; Schaffer, G. B.; Qian, M.; *Mat. Lett.*, **2014**, *132*, 196.
18. Li, X. P.; Yan, M.; Schaffer, G.B.; Qian, M.; *Intermetallic*, **2013**, *39*, 69.
19. Shen, B.; Inoue, A.; Kimura, H.; Omori, M.; Okubo, A.; *Mater. Sci. Eng. A*, **2004**, *375*, 666.
20. Kim, C. K.; Lee, S.; Shin, S. Y.; Kim, D. H.; *J. Alloy. Compd.*, **2008**, *453*, *108*.
21. Longhin, M.; Viennois, R.; Ravot, D.; Robin, J. J; Papet, P.; *Solid. State Science.*, **2014**, *38*, 129.
22. Dittrich, M.; Schumacher, G.; *Mater. Sci. Eng. A*, **2014**, *604*, 27.
23. Raghavan, V.; *Material Science and Engineering*; Prentice-Hall of India Private Limited Press New Delhi, INDIA, **1993**.
24. Gu, X.J.; Wang, J.Q.; Ye, F.; Lu, K.; *J. non-cryst. Solid*, **2001**, *296*, 74.
25. Maurya, R. S.; Sahu. A.; Laha, T.; *Mater. Sci. Eng. A*, **2016**, *649*, 48.
26. Zheng, B.; Ashford, D.; Zhou, Y.; Mathaudhu, S. N.; Delplanque, J.; Lavernia, E. J.; *Acta. Mater.*, **2013**, *61*, 4414.
27. Miracle, D. B.; Sanders, W.S.; Senkov, O. N.; *Phil. Mag.*, **2003**, *83*, 2409.
28. Jiang, J. Z.; Zhou, T. J.; Rasmussen, H.; Kuhn, U.; Eckert, J.; Lathe, C.; *Appl. Phys. Lett.*, **2000**, *77*, 3553.
29. Wang, W.H.; He, D. W.; Zhao, D. Q.; Yao, Y. S.; He, M.; *Appl. Phys. Lett.*, **1999**, *75*, 2770.
30. Jiang, J. Z.; Olsen, J. S.; Gerward, L.; Abdali, S.; Eckert, J.; Boer, N.S.; Schultz, L.; Truckenbrodt, J.; Shi, P. X.; *J. Appl. Phys.*, **2000**, *87*, 2664.
31. Spaepen, F.; Turnbull, D.; *Scripta. Metall.*, **1991**, *25*, 1563.
32. Chawake, N.; Pinto, L.D.; Srivastav, A. K.; Akkiraju, K.; Murty, B.S.; Kottada, R. S.; *Sci. Mater.*, **2014**, *93*, 52.
33. Groza, Z. R. Zavaliangos, A.; *Mater. Sci. Eng. A*, **2000**, *287*, 171.
34. German, R. M.; *Powder Metallurgy Science*; Metal Powder Industries Federation, Princeton; NJ: USA, **1989**.
35. Sasaki, T. T.; Hono, K.; Vierke, J.; Wollgarten, M.; Banhart, J.; *Mater. Sci. Eng. A*, **2008**, *490*, 343.

.